How many of the scaling trends in pp collisions will be violated at $\sqrt{s_{\mathrm{NN}}} = 14$ TeV? Predictions from Monte Carlo quark-gluon string model

J. Bleibel,[1,2] L. V. Bravina,[3,4,5] and E. E. Zabrodin[6,3,4,5]

[1]*Institut für Angewandte Physik, Universität Tübingen, Auf der Morgenstelle 10, D-72076 Tübingen, Germany*

[2]*Max-Planck-Institut für Intelligente Systeme, Heisenbergstr. 3, D-70569 Stuttgart, Germany*

[3]*Department of Physics, University of Oslo, PB 1048 Blindern, N-0316 Oslo, Norway*

[4]*National Research Nuclear University "MEPhI" (Moscow Engineering Physics Institute), Kashirskoe highway 31, Moscow RU-115409, Russia*

[5]*Frankfurt Institute for Advanced Studies, Ruth-Moufang-Straße 1, D-60438 Frankfurt a.M., Germany*

[6]*Skobeltzyn Institute for Nuclear Physics, Moscow State University, RU-119899 Moscow, Russia*

(Received 11 November 2010; published 10 June 2016)

Multiplicity, rapidity and transverse momentum distributions of hadrons produced both in inelastic and nondiffractive pp collisions at energies from $\sqrt{s} = 200$ GeV to 14 TeV are studied within the Monte Carlo quark-gluon string model. Good agreement with the available experimental data up to $\sqrt{s} = 13$ TeV is obtained, and predictions are made for the collisions at top LHC energy $\sqrt{s} = 14$ TeV. The model indicates that Feynman scaling and extended longitudinal scaling remain valid in the fragmentation regions, whereas strong violation of Feynman scaling is observed at midrapidity. The Koba-Nielsen-Olesen (KNO) scaling in multiplicity distributions is violated at LHC also. The origin of both maintenance and violation of the scaling trends is traced to short range correlations of particles in the strings and interplay between the multistring processes at ultrarelativistic energies.

DOI: 10.1103/PhysRevD.93.114012

I. INTRODUCTION

The recent interest in general features of elementary hadronic interactions, especially in characteristics of pp collisions, at ultrarelativistic energies is manifold. First of all, these collisions are conventionally used as reference ones to reveal the nuclear matter effects, such as strangeness enhancement, nuclear shadowing, collective flow, etc., attributed to formation of a pattern of hot and dense nuclear matter and the quark-gluon plasma (QGP) in the course of ultrarelativistic heavy-ion collisions (see [1] and references therein). Although the formation of the QGP and/or collective behavior was not found yet in pp collisions at energies up to the Tevatron energy $\sqrt{s} = 1.8$ TeV, strong evidence for azimuthal correlations up to $\sqrt{s} = 7$ TeV has been reported [2], and physicists are discussing the possibility to observe, e.g., elliptic flow in pp interactions at $\sqrt{s} = 7$ TeV and $\sqrt{s} = 13$ TeV accessible for the Large Hadron Collider (LHC) at CERN at present. This limit may be raised to $\sqrt{s} = 14$ TeV in the nearest future. Because of the huge amount of energy deposited in the overlapping region, the pp systems might be similar to $A + A$ collisions at a nonzero impact parameter at lower energies [3,4] and, therefore, demonstrate collectivity. An alternative approach developed in [5] considers the flow effects in hadronic interactions as initial state effects linked to correlation between the transverse momentum and position in the transverse plane of a parton in a hadron. In a recent paper [6] the authors argue that elliptic flow in pp collisions stems from the density variation mechanism within the color glass condensate (CGC) saturation physics. This important problem should definitely be clarified in the future.

Then, the problem of multiparticle production in elementary hadronic collisions is not fully solved yet. Here, for hard processes with large momentum transfer, the running coupling constant α_S is small, and that allows for application of the perturbative quantum chromodynamics (QCD). For soft processes with small momentum transfer, which give dominant contribution to high energy hadronic interactions, the α_S is close to unity, and therefore, nonperturbative methods should be applied. Many microscopic models [7–17] based on the string picture of particle production [18] have been successfully employed to describe gross features of hadronic collisions at relativistic and ultrarelativistic energies, whereas the statistical approach pioneered more than 50 years ago by Fermi and Landau [19,20] is not ruled out. To make predictions for the LHC in the latter case, one has to extrapolate the data obtained at lower energies to the high energy region. It was found quite long ago that, despite the complexity of a reaction with tens or more particles in a final state, multiparticle production in pp collisions exhibits several universal trends, such as $(\ln\sqrt{s})^2$ dependence of total charged particle multiplicity [21], Feynman scaling [22] and related to it extended longitudinal scaling [23], Koba-Nielsen-Olesen (KNO) scaling [24], and so forth. Similar trends were found later on in proton-nucleus and

nucleus-nucleus collisions as well (for review see, e.g., [25]). On the other hand, the description of ultrarelativistic hadronic interactions in the framework of color glass condensate theory [26] leads to a universal power-law behavior of, e.g., density of produced charged particles per unit of rapidity and their transverse momentum [27,28].

The aim of the present article is to study the main characteristics of pp interactions at energies from $\sqrt{s} =$ 200 GeV to top LHC energy $\sqrt{s} = 14$ TeV. We employ the Monte Carlo (MC) realization [9] of the quark-gluon string model (QGSM) [29] based on Gribov's Reggeon field theory (RFT) [30] that obeys both analyticity and unitarity requirements. The features of the model are described in Sec. II in detail. Comparisons with available experimental data for $\bar{p}p$ and pp collisions at energies $\sqrt{s} \geq 200$ GeV, including the measurements at LHC for pp interactions at $\sqrt{s} = 2.36$ TeV, $\sqrt{s} = 7$ TeV, and the recently measured $\sqrt{s} = 13$ TeV, as well as predictions for the top LHC energy $\sqrt{s} = 14$ TeV, are presented in Sec. III. Here, exclusive contributions of soft and hard processes to particle rapidity and transverse momentum spectra are studied. Special attention is given to the origin of violation of the KNO scaling, violation of the Feynman scaling at midrapidity, and its maintenance in the fragmentation region. Obtained QGSM results are also confronted to the predictions of other microscopic and macroscopic models. Conclusions are drawn in Sec. IV.

II. QUARK-GLUON STRING MODEL AND ITS MONTE CARLO REALIZATION

As was mentioned in the Introduction, the description of soft hadronic processes cannot be done within the perturbative QCD. Therefore, similarly to the dual parton model [10], the quark-gluon string model [29] employs the so-called $1/N$ series expansion [31,32] of the amplitude for processes in QCD, where N is either number of colors N_c [31] or number of flavors N_f [32]. In this approach the amplitude of a hadronic process is represented as a sum over diagrams of various topologies, so the method is often called *topological expansion*. It appears that at high energies and small momentum transfer the arising diagrams are similar [33,34] to processes describing the exchange of Regge singularities in the t-channel. For instance, planar diagrams correspond to the exchange of Reggeons, and cylinder diagrams correspond to reactions without quantum number exchange in the t-channel, i.e., taking place via the Pomeron exchange, where Pomeron is a composite state of the Reggeized gluons. Processes with many-Pomeron or many-Reggeon exchanges are also possible. To find the amplitude of multiparticle production, one has to cut the diagrams in the s-channel, and the physical picture of quark-gluon strings arises. Namely, new particles are produced through the formation and breakup of quark-gluon strings or exited objects consisting of quarks, diquarks and their antistates connected by a gluon string.

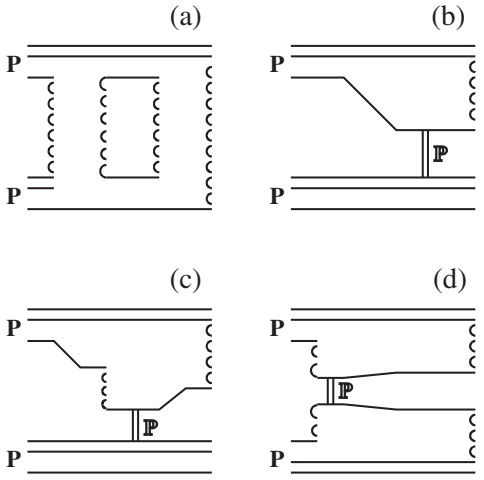

FIG. 1. Diagrams of particle production processes included in the modeling of pp interactions at ultrarelativistic energies. See text for details.

Figure 1 shows the subprocesses with particle creation taken into account in the current Monte Carlo version of the QGSM [9] for pp collisions at ultrarelativistic energies. The inelastic cross section consists of three terms

$$\sigma_{\text{inel}}^{pp}(s) = \sigma_P(s) + \sigma_{SD}(s) + \sigma_{DD}(s), \tag{1}$$

where $\sigma_P(s)$ is the cross section for the multichain processes described by the cylinder diagram and diagrams with multi-Pomeron scattering [Fig. 1(a)], $\sigma_{SD}(s)$ is the cross section of single-diffractive processes represented by the diagrams with small [Fig. 1(b)] and large [Fig. 1(c)] mass excitation, corresponding to the triple-Reggeon and triple-Pomeron limit, respectively, and $\sigma_{DD}(s)$ is the cross section of the double-diffractive process shown by the diagram in Fig. 1(d). Other diagrams that are relevant at low and intermediate energies, such as the undeveloped cylinder diagram or diagram with quark rearrangement [9], play a minor role here because their cross sections rapidly drop with rising s. The statistical weight of each subprocess is expressed in terms of the interaction cross section for the given subprocess $\sigma_i(s)$,

$$\omega_i = \sigma_i(s)/\sigma_{\text{inel}}(s). \tag{2}$$

Then, the hadron inelastic interaction cross section $\sigma_{\text{inel}}(s) = \sigma_{\text{tot}}(s) - \sigma_{el}(s)$ is split into the cross section for single-diffractive interactions $\sigma_{SD}(s)$ and the cross section for nondiffractive reactions $\sigma_{ND}(s)$, as is usually done in analysis of experimental data. By means of the Abramovskii-Gribov-Kancheli (AGK) cutting rules [35], the inelastic nondiffractive interaction cross section $\sigma_{ND}(s)$ can be expressed via the sum of the cross sections for the production of $n = 1, 2, \ldots$ pairs of quark-gluon strings, or cut Pomerons, and the cross section of double-diffractive process,

$$\sigma_{ND}(s) = \sum_{n=1}^{\infty} \sigma_n(s) + \sigma_{DD}(s). \quad (3)$$

To find $\sigma_n(s)$, one can rely on the quasi-eikonal model [34,36] which states that

$$\sigma_{\rm tot}(s) = \sum_{n=0}^{\infty} \sigma_n(s) = \sigma_P f\left(\frac{z}{2}\right), \quad (4)$$

$$\sigma_n(s) = \frac{\sigma_P}{nz}\left[1 - \exp(-z)\sum_{k=0}^{n-1}\frac{z^k}{k!}\right], \qquad k \geq 1, \quad (5)$$

$$\sigma_0 = \sigma_P\left[f\left(\frac{z}{2}\right) - f(z)\right], \quad (6)$$

$$f(z) = \sum_{\nu=1}^{\infty} \frac{(-z)^{\nu-1}}{\nu\nu!}. \quad (7)$$

Here,

$$\sigma_P = 8\pi\gamma_P \exp(\Delta\xi), \quad (8)$$

$$z = \frac{2C\gamma_P}{(R_P^2 + \alpha'_P\xi)} \exp(\Delta\xi). \quad (9)$$

The cross section σ_0 corresponds to diffraction contribution. The parameters γ_P and R_P are Pomeron-nucleon vertex parameters, quantity $\Delta \equiv \alpha_P(0) - 1$, and $\alpha_P(0)$ and α'_P are the intercept and the slope of the Pomeron trajectory, respectively. The quantity C takes into account the deviation from the pure eikonal approximation ($C = 1$) due to intermediate inelastic diffractive states, $\xi = \ln(s/s_0)$, and s_0 is a scale parameter.

For the diffractive processes displayed in Figs. 1(b) and 1(c), the fractions of momenta of initial hadrons carried by the sea quark pairs $x_{q\bar{q}}$ are determined according to distribution

$$u^h_{q\bar{q}}(x_{q\bar{q}}) \propto \frac{1 - x_{q\bar{q}}}{x_{q\bar{q}}^{1+\Delta}}. \quad (10)$$

Here, we use a simple model in which the soft $q\bar{q}$ pair is produced from a soft gluon emitted directly by a valence quark (the so-called first approximation). Thus, the proportionality coefficient in Eq. (10) is not directly related to the triple Pomeron vertex and should be fixed from the comparison with experimental data. The transverse momentum distribution of (anti)quarks in a proton in the low-mass excitation process shown in Fig. 1(b) is given by

$$f_q(\vec{p}_{\rm T})dp_{\rm T} = \frac{b_1}{\sqrt{\pi}} \exp(-b_1 p_{\rm T}^2) d\vec{p}_{\rm T}, \quad (11)$$

where the slope parameter $b_1 = 20\ ({\rm GeV}/c)^{-2}$. Then, it is assumed that the valence (anti)diquark in the (anti)proton carries a transverse momentum equal in magnitude and opposite in sign to the sum of transverse momenta of the other (anti)quarks. The number of quark-gluon strings increases with collision energy; thus, the average transverse momentum of the (anti)diquark rises also.

The quantitative description of single-diffractive and double-diffractive processes at high energies was done in QGSM in terms of dressed triple-Reggeon and loop diagrams [37,38]. The results obtained in [37] for the cross sections of the diffractive processes are utilized in our MC model via the parametrizations

$$\sigma_{SD}(s) = 0.68\left(1 + \frac{36}{s}\right)\ln(0.6 + 0.2s), \quad (12)$$

$$\sigma_{DD}(s) = 1.65 + 0.27\ln s. \quad (13)$$

Although these parametrizations are phenomenological, they agree well with the asymptotics $\sigma_D \propto \ln s$ corresponding to the Froissart bound, $\sigma_{\rm tot} \propto (\ln s)^2$.

Soft processes dominate the particle production in hadronic interactions at intermediate energies. With the rise of the collision energy, hard processes, resulting in formation of hadronic jets with large transverse momenta, become important also. To take into account the jet formation and, on the other hand, to describe simultaneously the increase of the total and inelastic hadronic interaction cross section with rising $\sqrt{s}$, the eikonal model was properly modified in [39] by introducing the new term that represents the hard Pomeron exchange. The cut of the hard Pomeron leads to formation of two hadronic jets, see Fig. 2. Therefore, the eikonal $u(s,b)$, that depends on the center-of-mass energy $\sqrt{s}$ and the impact parameter b, can be decomposed onto the terms corresponding to soft and hard Pomeron exchange:

$$u(s,b) = u_{\rm soft}(s,b) + u_{\rm hard}(s,b). \quad (14)$$

The inelastic hadronic cross section $\sigma_{\rm inel}(s)$ is connected to the real part of the eikonal $u^R(s,b)$ as

$$\sigma_{\rm inel}(s) = 2\pi\int_0^{\infty}\{1 - \exp[-2u^R(s,b)]\}bdb. \quad (15)$$

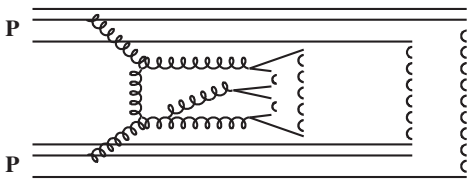

FIG. 2. String formation in hard gluon-gluon scattering and soft Pomeron exchange in proton-proton collision.

Recall that the concept of a (semi)hard Pomeron is nowadays a common feature of all RFT-based MC models [10,14–16,40] designed for the description of hadronic and nuclear interactions at ultrarelativistic energies. Other microscopic MC models also rely on the picture of a soft + hard eikonal approach [12].

Following [39,40], both soft and hard eikonals can be expressed as

$$u^R_{\text{soft/hard}}(s,b) = z_{\text{soft/hard}}(s)\exp\left[-\frac{\beta^2}{4\lambda_{\text{soft/hard}}(s)}\right], \quad (16)$$

where [cf. Eqs. (4)–(9)]

$$z_{\text{soft/hard}}(s) = \frac{\gamma_P}{\lambda_{\text{soft/hard}}(s)}\left(\frac{s}{s_0}\right)^{\alpha_P(0)-1}, \quad (17)$$

$$\lambda_{\text{soft/hard}}(s) = R_P^2 + \alpha'_P \ln\left(\frac{s}{s_0}\right). \quad (18)$$

Numerical values of the slopes and intercepts of the Pomeron trajectories and parameters of the hadron coupling to the Pomeron used in the model fit to experimental data are listed in Table I. Note that these values deviate from the parameters of the soft and hard Pomerons obtained in [39,41] from the cross section of minijets measured by the UA1 Collaboration. To describe the LHC data at energies above $\sqrt{s} = 900$ GeV, it was necessary to increase the soft Pomeron intercept to $\alpha_P(0) - 1 \approx 0.156$ and to increase the slope parameter α'_P to 0.25.

For the hard Pomeron, the fractions of momenta of the gluons are generated from the structure function [42],

$$xG(x,Q^2) = C_g(\bar{s})x^{\eta_1^g(\bar{s})}(1-x)^{\eta_2^g(\bar{s})}, \quad (19)$$

with

$$\bar{s} = \ln\left[(\ln Q^2/\Lambda)/(\ln Q_0^2/\Lambda)\right], \qquad \Lambda = 200\ \text{MeV} \quad (20)$$

and

$$C_g(\bar{s}) = 2.01 - 3.56\bar{s} + 1.98\bar{s}^2, \quad (21)$$

$$\eta_1^g(\bar{s}) = -1.13\bar{s} + 0.48\bar{s}^2, \quad (22)$$

TABLE I. Parameters of the soft and hard Pomerons used in the current version of the QGSM.

Parameter	Soft Pomeron	Hard Pomeron
$\alpha_P(0)$	1.15615	1.3217
α'_P	0.25	0
γ_P	1.27475	0.021
R_P	2.0	2.4

$$\eta_2^g(\bar{s}) = 2.9 + 0.813\bar{s}. \quad (23)$$

The transverse momentum is generated from the distribution

$$f(p_T)dp_T = \alpha(1+p_T)^\beta, \quad (24)$$

where α and β are determined for each event by fitting the summed cross sections (calculated from Ref. [43] for $y_1 = y_2 = 0$) for all $gg \to gg$ and $gg \to q\bar{q}$ processes, i.e., for all hard Pomerons, to an envelope

$$\frac{d^3\sigma}{dp_T^2 dy_1 dy_2} \lesssim \alpha(1+p_T)^\beta. \quad (25)$$

The p_T values are then generated within the following limits:

$$p_{T,\min}(s) = p_{T,0} + 0.0054s^{0.31393}, \quad (26)$$

$$p_{T,\max}(s) = p_{T,\min}(s) + 6.0 + 0.08s^{\alpha_P^{\text{hard}}(0)-1}. \quad (27)$$

This procedure generates an explicit dependence of the transverse momentum of the produced particles on the collision energy $\sqrt{s}$. As $\sqrt{s}$ increases, more and more hard Pomerons emerge. The differential cross section given by Eq. (25) increases, rendering the power-law distribution for p_T harder, with additionally increased lower and upper cutoff values for the distribution.

Then, the AGK cutting rules enable one to express the inelastic cross section as

$$\sigma_{\text{inel}}(s) = \sum_{i,j=0;i+j\geq 1}\sigma_{ij}(s), \quad (28)$$

where

$$\sigma_{ij}(s) = 2\pi\int_0^\infty bdb\exp\left[-2u^R(s,b)\right] \times \frac{[2u^R_{\text{soft}}(s,b)]^i}{i!}\frac{[2u^R_{\text{hard}}(s,b)]^j}{j!}. \quad (29)$$

The last expression can be used to determine the number of quark-gluon strings and hard jets via the number of cut soft and hard Pomerons, respectively. At very high energies, one has to take into account the effects of shadowing of partonic distributions both in nucleons and in nuclei. In the Reggeon calculus such processes correspond to the so-called enhanced diagrams [44] describing the interactions between Pomerons. These diagrams are not implemented yet in the current MC version of the QGSM.

As has been discussed in the literature (see, e.g., Refs. [45–47]), the AGK cutting rules are violated for multiple gluon production from Pomeron vertices. In our model, however, the number of gluons produced from a

single hard Pomeron vertex is limited to two. Therefore, an exchange of a hard Pomeron leads only to $gg \to gg$ or $gg \to q\bar{q}$ processes, i.e., only a double-gluon emission from a hard Pomeron may happen. As was pointed out in [46], the AGK cutting rules provide the leading contribution for the inclusive double-gluon emission process.

The multi-Pomeron exchanges become very important with increasing c.m. energy of hadronic collision. For instance, the contribution of a single-cylinder diagram to the scattering amplitude is proportional to $(s/s_0)^{\alpha_P(0)-1}$, $\alpha_P(0) > 0$. In contrast, the contributions coming from the n-Pomeron exchanges grow as $(s/s_0)^{n\Delta}$. Although in the framework of the $1/N$-expansion the n-Pomeron exchange amplitudes are suppressed by factor $1/N^{2n}$, the quickly rising term $s^{n\Delta}$ dominates over the suppression factor at ultrarelativistic energies.

There is no unique theoretical prescription for modeling the fragmentation of a string with a given mass, momentum and quark content into hadrons. In the presented version of the QGSM the Field-Feynman algorithm [48] is employed. It enables one to consider emission of hadrons from both ends of the string with equal probabilities. The breakup procedure invokes the energy-momentum conservation and the preservation of the quark numbers. The transverse momentum of the (di)quarks in the vacuum pair is determined by the power-law probability

$$f(p_T^2)dp_T^2 = \frac{3Db_2(s)}{\pi(1+Dp_T^2)^4}dp_T^2, \tag{30}$$

$$b_2(s) = 0.325 + 0.016\ln s, \tag{31}$$

with $D = 0.34\ (\mathrm{GeV}/c)^{-2}$.

Further details of the MC version of QGSM and its extension to $h+A$ and $A+A$ collisions can be found in [9,49,50].

III. COMPARISON WITH DATA AND PREDICTIONS FOR LHC

A. Cross sections

For the comparison with model results concerning the pseudorapidity and transverse momentum distributions, we used experimental data obtained by the UA5 Collaboration for antiproton-proton collisions at c.m. energies $\sqrt{s} =$ 200 GeV, 546 GeV and 900 GeV [51], by the UA1 Collaboration for $\bar{p}p$ collisions at $\sqrt{s} = 546$ GeV [52], by the CDF and the E735 Collaborations for $\bar{p}p$ collisions at $\sqrt{s} = 1800$ GeV [53,54], and recent CERN LHC data obtained for pp interactions at $\sqrt{s} = 900$ GeV, 2360 GeV, 7 TeV, 8 TeV and 13 TeV by the ALICE Collaboration [55–59], by the CMS Collaboration [60–62], and by the TOTEM Collaboration [63]. At such high energies, the annihilation cross section is almost zero, and the main characteristics of particle production in pp and $\bar{p}p$ interactions are essentially similar.

TABLE II. Total, elastic, multichain, single-diffraction and double-diffraction cross sections of pp collisions calculated by the QGSM.

$\sqrt{s}$ (GeV)	σ_{tot} (mb)	σ_{el} (mb)	σ_P (mb)	σ_{SD} (mb)	σ_{DD} (mb)
200	51.62	9.67	31.12	6.12	4.51
546	60.83	12.51	35.72	7.48	5.05
630	62.25	12.97	36.42	7.67	5.13
900	65.85	14.15	38.19	8.16	5.32
1800	72.97	16.55	41.61	9.10	5.70
2360	75.74	17.50	42.92	9.47	5.84
7000	86.60	21.31	47.91	10.95	6.43
14000	93.07	23.61	50.76	11.89	6.80

Total and elastic cross sections are listed in Table II together with the cross sections of multichain, single- and double-diffraction processes for energies ranging from $\sqrt{s} = 200$ GeV to $\sqrt{s} = 14$ TeV. Compared to those at $\sqrt{s} = 900$ GeV, σ_{tot}, σ_{el} and σ_{SD} increase at $\sqrt{s} = 14$ TeV by nearly 50%, whereas σ_{DD} increases by less than 30%. For better understanding of theoretical uncertainties, the results obtained for the σ_{tot}, σ_{el}, σ_{SD} and σ_{DD} are compared in Fig. 3 with the available predictions of other models [16,64–67], which also rely on the RFT. We see that for Tevatron energy $\sqrt{s} = 1.8$ TeV, all models agree within 5% accuracy limit for all but double-diffraction cross section. At top LHC energy $\sqrt{s} = 14$ TeV, the predictions

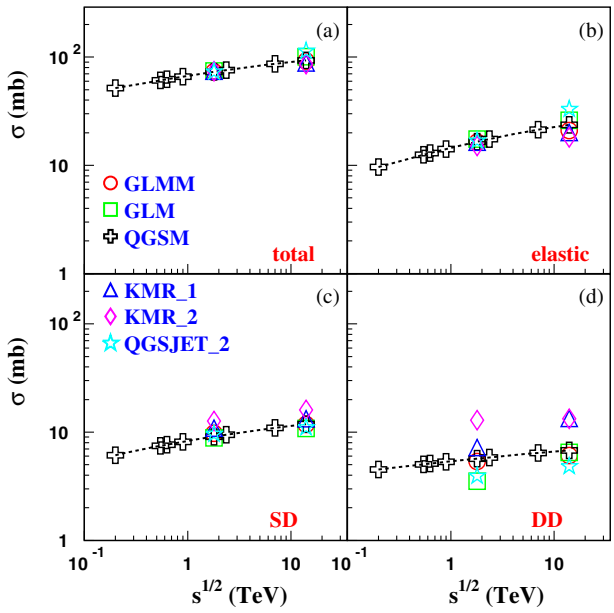

FIG. 3. (a) Total, (b) elastic, (c) single-diffractive and (d) double-diffractive cross sections as functions of $\sqrt{s}$ obtained in the models GLMM (circles) [64], GLM (squares) [65], QGSM (crosses), KMR-1 (triangles) [66], KMR-2 (diamonds) [67], and QGSJET-2 (stars) [16]. Dashed line, connecting the QGSM points, is drawn to guide the eye.

TABLE III. Inelastic, elastic, single-diffractive and double-diffractive cross sections of pp collisions measured at the LHC.

$\sqrt{s}$ (TeV)	$\sigma_{\rm inel}$ (mb)	σ_{el} (mb)	σ_{SD} (mb)	σ_{DD} (mb)
0.9 (ALICE) [68]	52.5		11.2	5.6
2.76 (ALICE)	62.8		12.2	7.8
7.0 (ALICE)	73.2		14.9	9.0
7.0 (LHCb) [70]	66.9			
7.0 (TOTEM) [69]	73.15	25.43		

for $\sigma_{\rm tot}$ and σ_{SD} are still close to each other, whereas the Durham models, KMR-1 and KMR-2, predict 50% excess of σ_{DD} compared to other models. Results of the present version of QGSM are close to the calculations of the GLMM model [64]. On the other hand, QGSM is like the QGSJET model [16], which also contains soft and hard Pomerons with the parameters similar to those listed in Table I except for the Pomeron slopes. QGSJET yields larger total and elastic cross sections at 14 TeV. A discussion of the similarities and differences between the models presented here can be found in [65].

Inelastic and diffractive cross sections have been measured at the LHC in [68–70]. The results are listed in Table III. After comparison of experimental data with the QGSM calculations from Table II, it turns out that the model works reasonably well. It tends to slightly underestimate most of the cross sections, although, e.g., the inelastic cross section in the model is quite close to the one reported by the LHCb Collaboration [70].

B. Transverse momentum spectra

The transverse momentum distributions of the invariant cross section $E\frac{d^3\sigma}{dp^3}$ divided to $\sigma_{\rm tot}$ for charged particles in nonsingle-diffractive (NSD) pp collisions at all energies in question are presented in Fig. 4. We see that the QGSM reproduces the experimental data in a broad energy range pretty well. The spectra become harder with increasing $\sqrt{s}$; thus, the average transverse momentum of produced hadrons should grow also. Figure 5 displays the $\langle p_{\rm T}\rangle$ of charged particles in NSD pp events calculated in QGSM and compared to experimental data. We assume here 5% systematic errors for the extraction of mean $p_{\rm T}$ because we do not apply any extrapolation procedure to the generated spectra, as it is usually done in the experiments. Results of the fit of model simulations to quadratic logarithmic dependence and to power-law dependence are as follows:

$$\langle p_{\rm T}\rangle = 0.417 - 0.0035\ln s + 0.00059\ln^2 s,$$
$$\langle p_{\rm T}\rangle = 0.243 + 0.12{\rm E}^{0.1107}.$$

In the last expression $E = \sqrt{s}/2$, and the exponent 0.1107 is not a free parameter. According to [28], this exponent is just half of the exponent of the power-law fit to $dN/d\eta$ distribution (see below). As one can see in Fig. 5, the

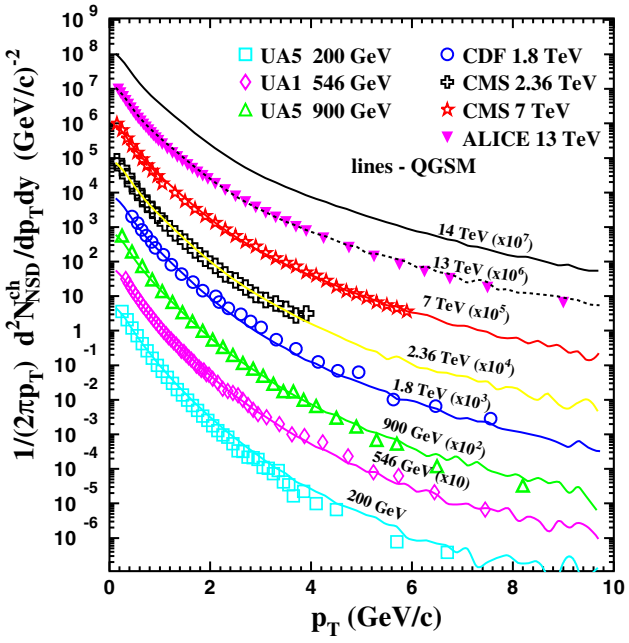

FIG. 4. Transverse momentum distributions of the invariant cross section of charged particles in NSD pp collisions obtained in QGSM at $|y| \le 2.5$ for all energies in question. Experimental data are taken from [51–53,59,61].

difference between the two parametrizations of mean $p_{\rm T}$ is negligible even for top LHC energy $\sqrt{s} = 14$ TeV.

To study the interplay between the soft and hard processes, we show separately in Fig. 6 their fractional contributions and combined results for pp collisions at $\sqrt{s} = 900$ GeV, 2.36 TeV, 7 TeV and at top LHC energy $\sqrt{s} = 14$ TeV. Moreover, the $p_{\rm T}$ dependence of the underlying soft processes from the collisions with at least one

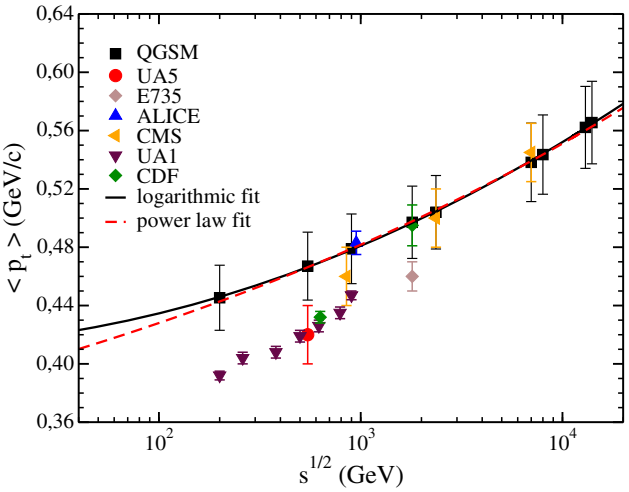

FIG. 5. Average transverse momentum as a function of $\sqrt{s}$. Squares present the QGSM results; other symbols denote experimental data from [51–54,57,61]. Solid and dashed lines are fit to logarithmic and power-law dependences, respectively. See text for details.

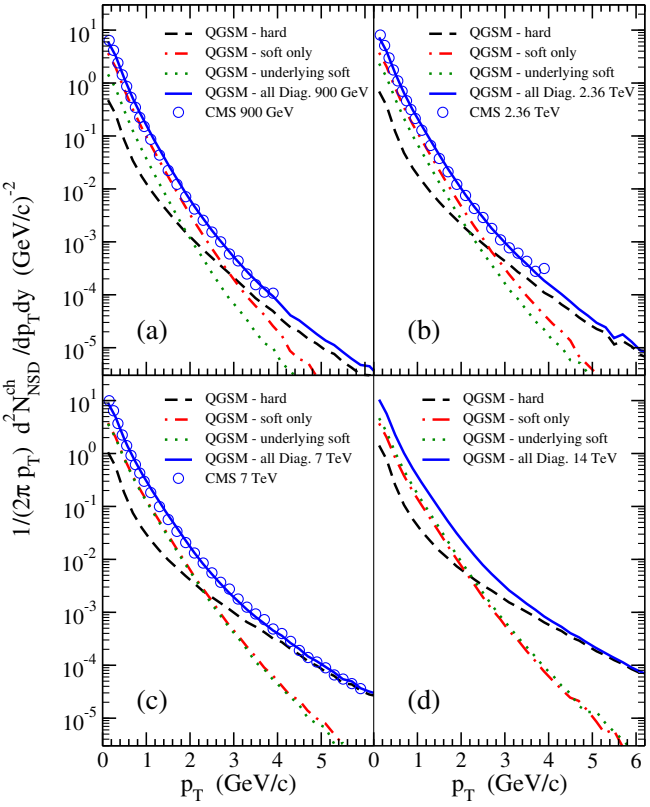

FIG. 6. Transverse momentum distributions of the invariant cross section of charged particles in NSD pp collisions at (a) $\sqrt{s} = 900$ GeV, (b) $\sqrt{s} = 2360$ GeV, (c) $\sqrt{s} = 7$ TeV and (d) $\sqrt{s} = 14$ TeV calculated in QGSM. Combined contribution of all processes and, separately, of only soft, hard and underlying soft subprocesses are shown by solid, dash-dotted, dashed and dotted lines, respectively (see text for details). Experimental data plotted in panels (a), (b) and (c) are taken from [60,61].

hard Pomeron is displayed in these plots as well as with the experimental data of the CMS Collaboration. As expected, the soft processes dominate at low and intermediate transverse momenta, whereas at higher transverse momenta the major contribution to the cross section comes from the minijets. The crossover between the hard and soft branches takes place at $p_T \approx 2.8$ GeV/c for the reactions at $\sqrt{s} =$ 900 GeV. It is shifted to $p_T \approx 2.2$ GeV/c at $\sqrt{s} = 14$ TeV. The slopes of the p_T spectra for both soft and underlying soft processes are similar. At $\sqrt{s} = 7$ TeV and 14 TeV, both lines coincide; i.e., the contributions to the invariant cross sections from barely soft Pomeron processes are equal to those from the soft Pomerons exchanges, accompanied by one or more hard Pomeron ones.

In view of these results it becomes clear what process generates the growing mean p_T in our model. Particle production from soft and hard Pomerons includes different distributions for the transverse momentum. Their relative contributions are energy dependent, see Fig. 6. Additionally, both distributions depend explicitly on the collision energy. With growing $\sqrt{s}$, more and more hard Pomerons are exchanged, rendering the spectra of secondaries harder.

C. Rapidity distributions

Let us briefly recall the main assumptions and predictions of the hypothesis of Feynman scaling [22]. It requires scaling behavior of particle spectra within the whole kinematically allowed region of the Feynman scaling variable $x_F \equiv p_{||}/p_{||}^{max}$ or, alternatively, c.m. rapidity y^* at ultrarelativistic energies $s \to \infty$. In addition, the existence of nonvanishing central area $|x_F| \le x_0$, $x_0 \sim 0.1$ is postulated. In terms of rapidity this central region increases with rising $\sqrt{s}$ as

$$(\Delta y^*)_{centr} \approx 2 \ln [x_0 \sqrt{s}/m_T] \tag{32}$$

provided the transverse mass $m_T = \sqrt{m_0^2 + p_T^2}$ is finite. In contrast, the fragmentation region remains constant

$$(\Delta y^*)_{frag} \approx \ln (1/x_0). \tag{33}$$

From here, it follows that (i) in the central area the particle density $\rho_{cent}(y^*, p_T, s)$ depends on neither y^* nor $\sqrt{s}$, i.e., $\rho_{cent} \equiv \rho_{cent}(p_T)$, and rapidity spectra of particles have, therefore, a broad plateau; (ii) this area gives a main contribution to average multiplicity of produced hadrons; (iii) contribution to the average multiplicity from the fragmentation regions is energy independent.

The charged particle pseudorapidity spectra $\frac{1}{\sigma_{inel}} \frac{d\sigma_{inel}}{d\eta}$ and $\frac{1}{\sigma_{NSD}} \frac{d\sigma_{NSD}}{d\eta}$ for inelastic and nonsingle-diffractive events, respectively, are displayed in Figs. 7(a) and 7(b) together with the $pp(\bar{p}p)$ data at $\sqrt{s} = 200$ GeV, 546 GeV, 900 GeV, 2.36 TeV, 7 TeV and 13 TeV. QGSM predictions for $\sqrt{s} = 14$ TeV are plotted here also. The model gives a good description of these distributions within the indicated energy range except, maybe, a not very distinct dip at midrapidity for the lowest energy in question $\sqrt{s} =$ 200 GeV. For pp collisions at top LHC energy, QGSM predicts a further increase of the central particle densities to

$$\left.\frac{dN_{inel}}{d\eta}\right|_{\eta=0} = 5.8, \qquad \left.\frac{dN_{NSD}}{d\eta}\right|_{\eta=0} = 6.7.$$

Compared to the $\sqrt{s} = 7$ TeV, the rise of the central particle density at $\sqrt{s} = 14$ TeV is expected to be about 20%.

In Fig. 8, the charged particle density at $\eta = 0$ is presented as a function of the c.m. energy $\sqrt{s}$ for inelastic (upper plot) and nonsingle-diffractive (bottom plot) events. The experimental data for inelastic collisions below $\sqrt{s} =$ 546 GeV are well described by a linear dependence on $\ln s$ [51]. The striking evidence of the first LHC results for pp interactions at $\sqrt{s} = 900$ GeV, 2.36 GeV and 7 TeV is the quadratic dependence of the increase of midrapidity density of charged particles with rising $\ln s$ [61]. The theory of CGC suggests a power-law rise [27,28]. In the QGSM these

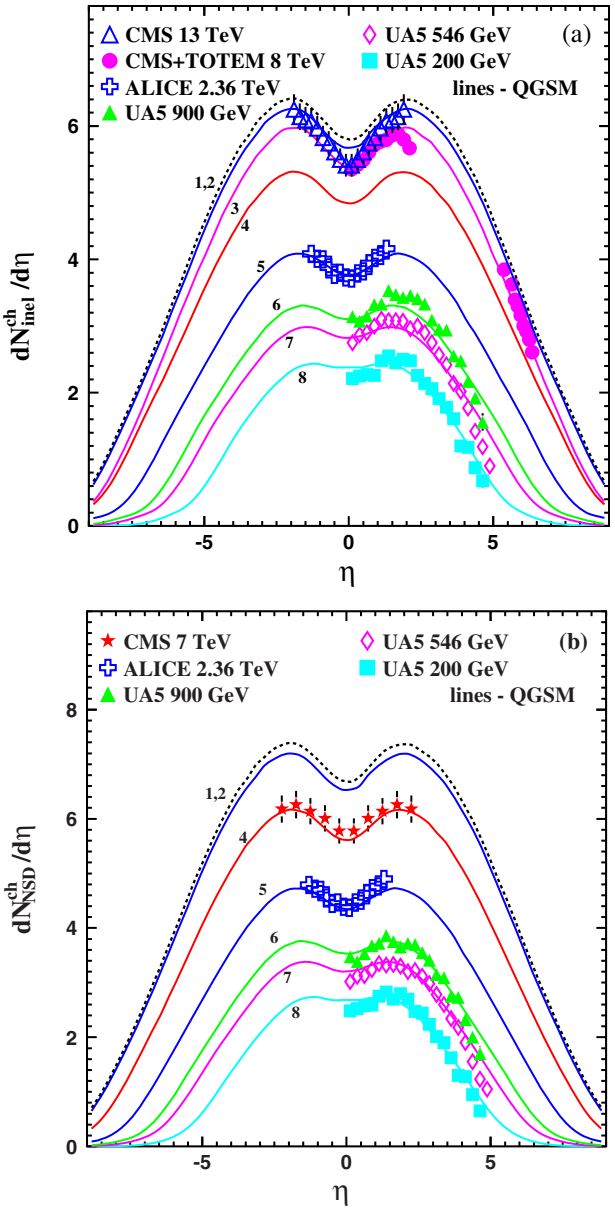

FIG. 7. The charged particle pseudorapidity spectra for (a) inelastic and (b) nonsingle-diffractive events calculated in QGSM for pp collisions at $\sqrt{s} = 200$ GeV (8), 546 GeV (7), 900 GeV (6), 2.36 TeV (5), 7 TeV (4), 8 TeV (3), 13 TeV (2), and 14 TeV (1). Data are taken from [51,56,59,61,62].

trends hold also, and the fitting parametrizations for c.m. energies from 200 GeV to 14 TeV are

$$\left.\frac{dN_{\rm inel}}{d\eta}\right|_{\eta=0}(s) = 4.36 - 0.507\ln s + 0.03\ln^2 s,$$

$$\left.\frac{dN_{\rm NSD}}{d\eta}\right|_{\eta=0}(s) = 5.015 - 0.60\ln s + 0.036\ln^2 s,$$

$$\left.\frac{dN_{\rm NSD}}{d\eta}\right|_{\eta=0}(s) = 0.77E^{0.22}.$$

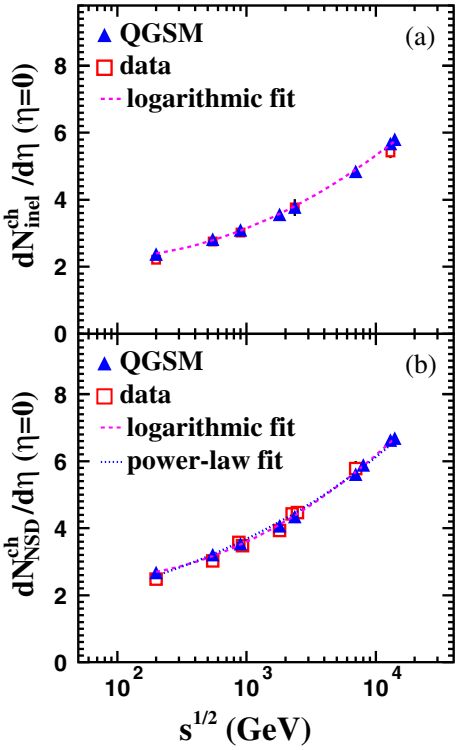

FIG. 8. The charged particle density at midrapidity as a function of $\sqrt{s}$ for (a) inelastic and (b) nonsingle-diffractive collisions. Dashed lines show the results of the fit to expression $a + b\ln s + c\ln^2 s$, dotted line (b) to the power-law dependence $d\sqrt{s}^{\lambda}$.

As in the mean $p_{\rm T}$ case, there is a hair's width difference between the two curves representing the logarithmic and the power-law fit, respectively. Indicating a further increase of particle density at $\eta = 0$ with rising energy, the model favors violation of the Feynman scaling at midrapidity; otherwise, the particle density there should not depend on $\sqrt{s}$.

It is interesting to compare the QGSM predictions for the charged particle multiplicity in pp collisions at LHC with that obtained by the extrapolation of pseudorapidity distributions measured at lower energies. This method [25] employs the energy independence of the slopes of the pseudorapidity spectra combined with logarithmic proportionality to $\sqrt{s}$ of both the width and the height of the distributions. Therefore, any data set from Figs. 7(a) and 7(b) can be used for the extrapolation, and the results are [25]

$$\left.\frac{dN_{\rm NSD}}{d\eta}\right|_{\eta=0} = 4.6 \pm 0.4, \qquad \left.\frac{dN_{\rm NSD}}{d\eta}\right|_{\eta=\pm 2} = 5.25 \pm 0.7.$$

These predictions are significantly lower than the recent experimental data from LHC and the QGSM calculations.

Another feature that is closely related to Feynman scaling is the so-called extended longitudinal scaling

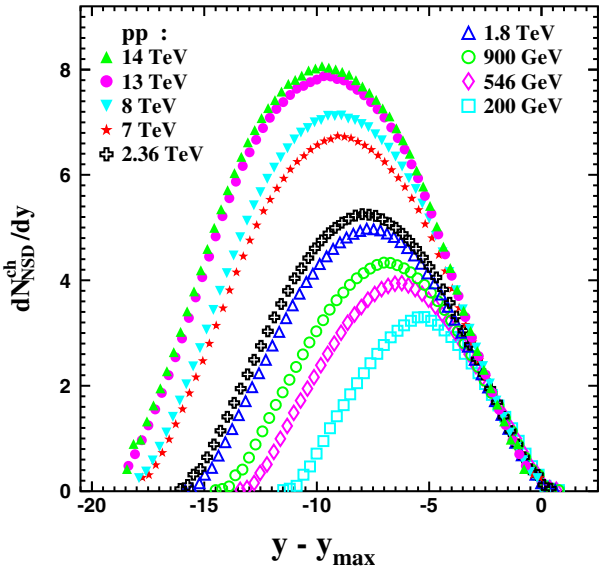

FIG. 9. The distributions $\frac{1}{\sigma_{\rm NSD}}\frac{d\sigma_{\rm NSD}}{dy}$ as functions of rapidity difference $y - y_{\rm max}$ obtained in QGSM for energies $\sqrt{s} = 200$ GeV, 546 GeV, 900 GeV, 1.8 TeV, 2.36 TeV, 7 TeV, 13 TeV and 14 TeV.

[23] exhibited by the slopes of (pseudo)rapidity spectra. In the QGSM these slopes are identical in the fragmentation region $y_{\rm beam} \geq -2.5$ as shown in Fig. 9, where the distributions $\frac{1}{\sigma_{\rm NSD}}\frac{d\sigma_{\rm NSD}}{dy}$ are expressed as functions $y - y_{\rm max}$. QGSM indicates that the extended longitudinal scaling remains certainly valid at LHC. This result contradicts the prediction based on the statistical thermal model [71]. The latter fits the measured rapidity distributions to the Gaussian, extracts the widths of the Gaussians and implements the energy dependence of the obtained widths to simulate the rapidity spectra at LHC. The extrapolated distribution was found to be much narrower [71] compared to that presented in Fig. 9. We are eagerly awaiting the LHC measurements of pp collisions in the fragmentation regions to resolve the obvious discrepancy. Note that experimentally the extended longitudinal scaling was found to hold to 10% in a broad energy range from $\sqrt{s} = 30.8$ GeV to 900 GeV [51].

The emergence of the extended longitudinal scaling as well as Feynman scaling in the QGSM is not accidental. It arises due to short range correlations in rapidity space. The correlation function of particle i and particle j, produced in the string fragmentation, drops exponentially with rising rapidity difference

$$C(y_i, y_j) = \frac{d^2\sigma}{\sigma_{\rm inel} dy_i dy_j} - \frac{d\sigma}{\sigma_{\rm inel} dy_i}\frac{d\sigma}{\sigma_{\rm inel} dy_j} \propto \exp\left[-\lambda(y_i - y_j)\right], \quad (34)$$

and therefore, the particles with large rapidity difference are uncorrelated. Consider now the inclusive process $1 + 2 \to i + X$. Its single particle inclusive cross section

$$f_i \equiv E\frac{d^3\sigma_i}{d^3p} = \frac{d^2\sigma(y_1 - y_i, y_i - y_2, p_{iT}^2)}{dy_i d^2 p_{iT}} \quad (35)$$

becomes independent of $y_i - y_2$ at sufficiently high collision energy in the fragmentation region of particle 1, provided $y_1 - y_i \approx 1$ and $y_i - y_2 \approx y_1 - y_2 \gg 1$. Thus, the inclusive densities $n_i \equiv f_i/\sigma_{\rm inel}$ are determined by only two variables

$$n_i = \phi(y_1 - y_i, p_{iT}^2). \quad (36)$$

Recalling that the Feynman variable x_F is connected to rapidity via

$$x_{iF} \equiv \frac{p_{i\|}}{p_{\|}^{\rm max}} \approx \exp\left[-(y_1 - y_i)\right], \quad (37)$$

one arrives from Eq. (23) to the condition of Feynman scaling

$$n_i = \psi(x_F^{(i)}, p_{iT}^2). \quad (38)$$

The invariant distribution

$$F(x_F) = \frac{2}{\pi\sqrt{s}}\int E_{cm}\frac{d^2\sigma}{dx_F dp_{\rm T}^2}dp_{\rm T}^2 \quad (39)$$

is displayed in Fig. 10 for all charged particles from the pp collisions at energies from $\sqrt{s} = 200$ GeV to 14 TeV. The scaling seems to hold within 20% of accuracy in the fragmentation region at $0.1 < x_F < 0.2$ only.

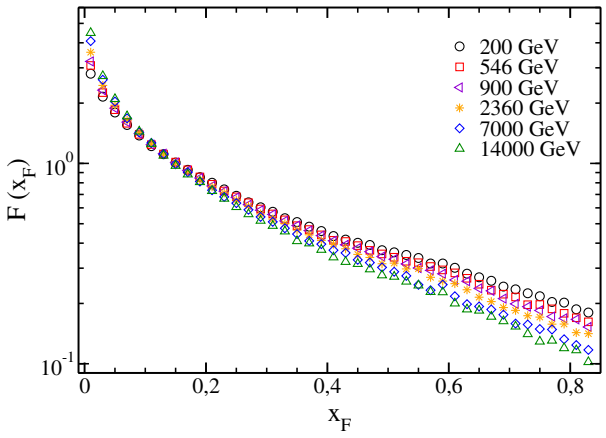

FIG. 10. The invariant distribution $F(x_{\rm F})$ in nonsingle-diffractive pp collisions obtained in QGSM at $\sqrt{s} = 200$ GeV, 546 GeV, 900 GeV, 1.8 TeV, 2.36 TeV and 14 TeV.

D. Violation of KNO scaling

Another scaling dependence is known as Koba-Nielsen-Olesen or KNO scaling [24]. Initially it was also derived from the hypothesis of Feynman scaling, but later on it appeared that both hypotheses are of independent origin. The KNO scaling claims that at $\sqrt{s} \to \infty$ the normalized multiplicity distribution just scales up as $\ln s$ or, equivalently, that

$$\frac{\langle n\rangle \sigma_n}{\Sigma \sigma_n} = \Psi\left(\frac{n}{\langle n\rangle}\right), \tag{40}$$

with σ_n being the partial cross section for n-particle production, $\langle n\rangle$ the average multiplicity and $\Psi(n/\langle n\rangle)$ energy independent function. KNO scaling was found to hold up to ISR energies, $\sqrt{s} \le 62$ GeV, despite the apparent failure of the Feynman scaling hypothesis in the central region $|x_F| \le x_0$. Violation of KNO scaling was predicted within the RFT in [29,35]. Later on the violation was observed experimentally by the UA5 and UA1 Collaborations in $\bar{p}p$ collisions at $\sqrt{s} = 546$ GeV [51]. The origin of this phenomenon in the model is the following. At ultrarelativistic energies the main contribution to particle multiplicity comes from the cut-Pomerons, and each cut results in formation of two strings. Short range correlations inside a single string lead to a Poisson-like multiplicity distribution of produced secondaries. At energies below 100 GeV, the multistring (or chain) processes are not very abundant and invariant masses of the strings are not very large. Therefore, different contributions to particle multiplicity overlap strongly, and KNO scaling is nearly fulfilled. With rising $\sqrt{s}$, the number of strings increases as $(s/s_0)^{\Delta}$, and their invariant masses increase as well. This leads to enhancement of high multiplicities, deviation of the multiplicity distribution from the Poisson-like behavior and violation of KNO scaling [9,29].

Before studying the violation of KNO scaling at LHC, we compare in Fig. 11 the QGSM calculations with the ALICE data. In this figure the multiplicity distributions of charged particles calculated in NSD pp events at $\sqrt{s} =$ 900 GeV and $\sqrt{s} = 2.36$ TeV in three central pseudorapidity intervals are plotted onto the experimental data. The agreement between the model results and the data is good. Moreover, the QGSM demonstrates a kind of a wavy structure mentioned in [56]. As we see below, such a wavy behavior in the model can be linked to processes going via the many-Pomeron exchanges.

The multiplicity distributions of charged particles obtained in QGSM for NSD pp collisions at all energies in question are presented in Fig. 12 for the interval $|\eta| < 2.4$. Although the differences between the neighbor energies seem not to be very dramatic, the tendency in the modification of the distributions is quite clear. The high-multiplicity tail is pushed up, maximum of the distribution is shifted towards small values of $n_{ch}/\langle n_{ch}\rangle$ and the

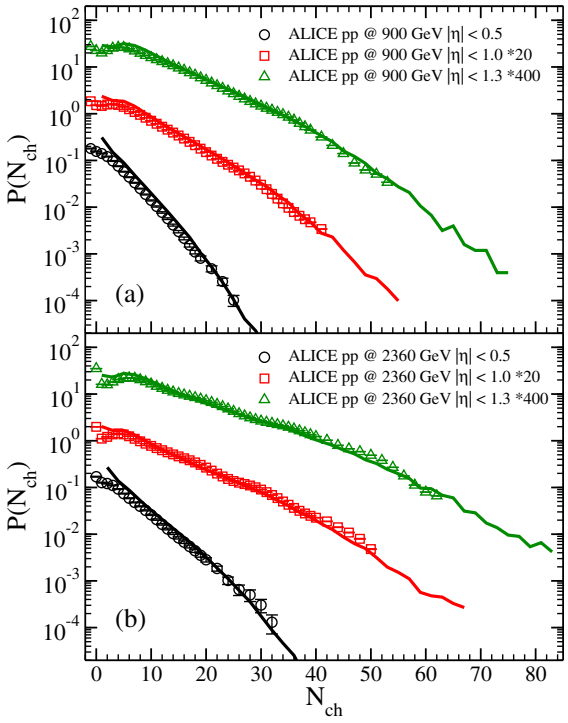

FIG. 11. Charged particle multiplicity distributions in $|\eta| < 0.5$, $|\eta| < 1.0$ and $|\eta| < 1.3$ intervals, obtained in QGSM for pp collisions at $\sqrt{s} = 900$ GeV (upper plot) and at $\sqrt{s} = 2360$ GeV (bottom plot). Open symbols show the corresponding ALICE data [56].

characteristic "shoulder" in the spectrum becomes quite distinct, as presented by the distribution for top LHC energy. Another interesting observation is the unique intersection point for all distributions. All curves cross each other at $z \approx 2.3$ as can be clearly seen in the bottom plot of Fig. 12, where the ratio $\langle n_{ch}\rangle P(z)|_{546\ \mathrm{GeV}}/\langle n_{ch}\rangle P(z)|_{7\ \mathrm{TeV}}$ is displayed. This prediction is in line with

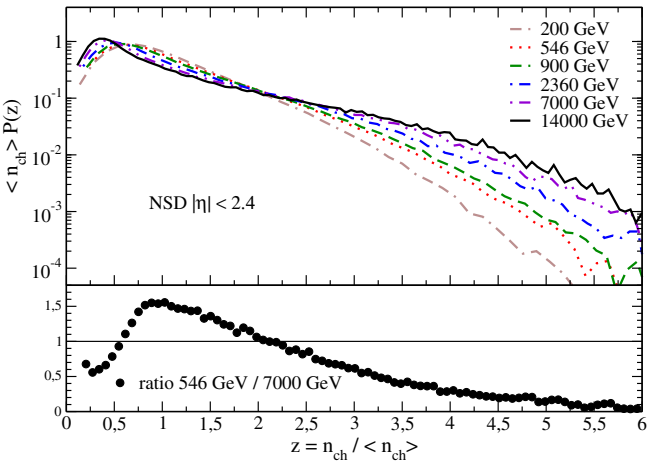

FIG. 12. Charged particle multiplicity distributions in the KNO variables in QGSM nondiffractive pp ($p\bar{p}$) collisions at $\sqrt{s} = 200$ GeV, 564 GeV, 900 GeV, 2.36 TeV, 7 TeV and 14 TeV.

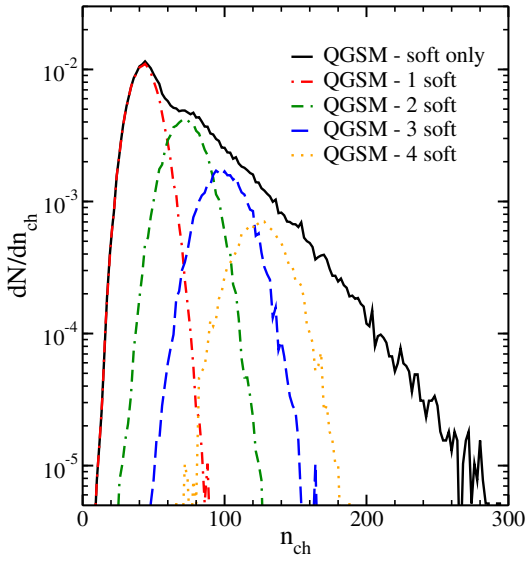

FIG. 13. Charged particle multiplicity distribution (solid line) for processes going via the exchange of $n \geq 1$ soft Pomerons in pp collisions at $\sqrt{s} = 14$ TeV. Contributions of the first four terms are shown by dash-dotted ($n = 1$), double-dash–dotted ($n = 2$), dashed ($n = 3$) and dotted ($n = 4$) lines, respectively.

a recent measurement of multiplicity distributions and investigation of KNO scaling [72], where the same qualitative behavior has now been observed. Note that the aforementioned pseudorapidity range $|\eta| < 2.4$ is not sufficient to observe the multihump structure in the KNO plot predicted in [34] (see also [38]) for the full phase space. To clarify the role of multi-Pomeron processes in violation of KNO scaling explicitly, Fig. 13 shows the contribution to the particle multiplicity diagram coming from the processes with different number of soft Pomerons in pp collisions at $\sqrt{s} = 14$ TeV. The maxima of distributions for multi-Pomeron processes are moved in the direction of high multiplicities thus lifting the high-multiplicity tail. The pronounced peak in the low-multiplicity interval arises solely due to single Pomeron exchange.

IV. CONCLUSIONS

Multiplicity, transverse momentum and (pseudo)rapidity distributions of hadrons produced in pp interactions at energies from $\sqrt{s} = 200$ GeV to 14 TeV are studied within the Monte Carlo quark-gluon string model. Parameters of soft and hard Pomerons are determined from the fit to recent LHC pp data. Compared to the fit to lower energies, it was found necessary both to increase the intercept of soft Pomeron and to reduce its slope parameter. Other parameters, such as total cross sections, cross sections of single-diffractive and double-diffractive processes, etc., are taken from theoretical considerations. The model simulations of pseudorapidity, transverse momentum and multiplicity spectra of secondaries are in a good agreement with the corresponding experimental data obtained in $\bar{p}p$ and pp collisions at Tevatron and at CERN energies. Predictions are made for pp interactions at top LHC energy $\sqrt{s} = 14$ TeV. We demonstrated how an increase of the mean p_T with energy is generated within our model due to the interplay of an increasing exchange of hard Pomerons and explicitly s-dependent p_T distributions during the string-break procedure. It is shown that within the examined energy range one cannot distinguish between the "standard" logarithmic dependence ($\propto \ln^2 s$) and novel power-law approximation ($\propto E^{\lambda}$), employed for particle densities and for their mean p_T in the present model, based on Reggeon Field theory, and in theory of color glass condensate, respectively.

Several scaling properties observed in particle production at relativistic energies have been examined. QGSM favors violation of Feynman scaling in the central rapidity region and its preservation in the fragmentation areas. Extended longitudinal scaling is shown to hold at LHC. This scaling is also attributed to heavy-ion collisions at energies up to $\sqrt{s} = 200$ GeV. Extrapolations based on statistical thermal model predict its violation at LHC, thus implying vanishing of Feynman scaling for nuclear collisions in the fragmentation regions as well. This important problem should be resolved experimentally in the nearest future. Finally, further violation of the KNO scaling in multiplicity distributions is demonstrated in QGSM. The origin of both conservation and violation of the scaling trends is traced to short range correlations of particles in the strings and interplay between the multi-Pomeron processes at ultrarelativistic energies.

ACKNOWLEDGMENTS

Fruitful discussions with K. Boreskov, L. Csernai, O. Kancheli, L. McLerran and S. Ostapchenko are gratefully acknowledged. This work was supported by the Norwegian Research Council (NFR) under Contract No. 185664/V30. J. B. thanks the German Research Foundation (DFG) for the financial support through the Project BL 1286/2-1. L. B. acknowledges financial support of the Alexander von Humboldt Foundation.

[1] *Proceedings of Quark Matter, 2014*, edited by P. Braun-Munzinger, B. Friman, and J. Stachel, [*Nucl. Phys.* **A931, 1c (2014)].**

[2] B. Abelev *et al.* (ALICE Collaboration), J. High Energy Phys. 09 (2013) 049.

[3] L. Cunqueiro, J. Dias de Deus, and C. Pajares, Eur. Phys. J. C **65**, 423 (2010).

[4] D. d'Enterria, G. Eyyubova, V. Korotkikh, I. Lokhtin, S. Petrushanko, L. Sarycheva, and A. Snigirev, Eur. Phys. J. C **66**, 173 (2010).

[5] K. G. Boreskov, A. B. Kaidalov, and O. V. Kancheli, Eur. Phys. J. C **58**, 445 (2008).

[6] E. Gotsman, E. Levin, U. Maor, and S. Tapia, Phys. Rev. D **93**, 074029 (2016).

[7] B. Andersson, G. Gustafson, and B. Nielsson-Almqvist, Nucl. Phys. **B281**, 289 (1987).

[8] H.-U. Bengtsson and T. Sjostrand, Comput. Phys. Commun. **46**, 43 (1987).

[9] N. S. Amelin and L. V. Bravina, Yad. Fiz. **51**, 211 (1990) [Sov. J. Nucl. Phys. **51**, 133 (1990)]; N. S. Amelin, L. V. Bravina, L. I. Sarycheva, and L. I. Smirnova, Yad. Fiz. **51**, 841 (1990) [Sov. J. Nucl. Phys. **51**, 535 (1990)].

[10] A. Capella, U. Sukhatme, C.-I. Tan, and J. Tran Thanh Van, Phys. Rep. **236**, 225 (1994).

[11] K. Werner, Phys. Rep. **232**, 87 (1993).

[12] M. Gyulassy and X. N. Wang, Comput. Phys. Commun. **83**, 307 (1994).

[13] M. Bleicher, E. Zabrodin, C. Spieles, S. A. Bass, C. Ernst, S. Soff, L. Bravina, M. Belkacem, H. Weber, H. Stöcker, and W. Greiner, J. Phys. G **25**, 1859 (1999).

[14] K. Werner, F.-M. Liu, and T. Pierog, Phys. Rev. C **74**, 044902 (2006).

[15] R. Engel, J. Ranft, and S. Roesler, Phys. Rev. D **52**, 1459 (1995).

[16] S. Ostapchenko, Nucl. Phys. B, Proc. Suppl. **151**, 143 (2006); Phys. Rev. D **83**, 014018 (2011).

[17] B.-H. Sa, D.-M. Zhou, Y.-L. Yan, X.-M. Li, S.-Q. Feng, B.-G. Dong, and X. Cai, Comput. Phys. Commun. **183**, 333 (2012).

[18] T. Sjöstrand, Comput. Phys. Commun. **39**, 347 (1986).

[19] E. Fermi, Prog. Theor. Phys. **5**, 570 (1950).

[20] L. D. Landau, Izv. Akad. Nauk SSSR, Ser. Fiz. **17**, 51 (1953); S. Z. Belenkij and L. D. Landau, Nuovo Cimento **3**, 15 (1956).

[21] C. Amsler *et al.* (Particle Data Group), Phys. Lett. B **667**, 1 (2008).

[22] R. Feynman, Phys. Rev. Lett. **23**, 1415 (1969); R. Feynman, *Photon-Hadron Interactions* (Benjamin, New York, 1972).

[23] G. J. Alner *et al.* (UA5 Collaboration), Z. Phys. **C33**, 1 (1986).

[24] Z. Koba, H. B. Nielsen, and P. Olesen, Nucl. Phys. **B40**, 317 (1972).

[25] W. Busza, J. Phys. G **35**, 044040 (2008).

[26] L. McLerran, Lect. Notes Phys. **583**, 291 (2002).

[27] E. Levin and A. H. Rezaeian, Phys. Rev. D **82**, 014022 (2010).

[28] L. McLerran and M. Praszalowicz, Acta Phys. Pol. B **41**, 1917 (2010).

[29] A. B. Kaidalov, Phys. Lett. **116B**, 459 (1982); A. B. Kaidalov and K. A. Ter-Martirosyan, Phys. Lett. **117B**, 247 (1982).

[30] V. Gribov, Sov. Phys. JETP **26**, 414 (1968); L. V. Gribov, E. M. Levin, and M. G. Ryskin, Phys. Rep. **100**, 1 (1983).

[31] G. t'Hooft, Nucl. Phys. **75**, 461 (1974).

[32] G. Veneziano, Phys. Lett. **52B**, 220 (1974).

[33] M. Cifaloni, G. Marchesini, and G. Veneziano, Nucl. Phys. **B98**, 472 (1975).

[34] A. B. Kaidalov, Surv. High Energy Phys. **13**, 265 (1999).

[35] V. Abramovskii, V. Gribov, and O. Kancheli, Yad. Fiz. **18**, 595 (1973) [Sov. J. Nucl. Phys. **18**, 308 (1974)].

[36] M. Baker and K. A. Ter-Martirosyan, Phys. Rep. **28C**, 1 (1976).

[37] A. B. Kaidalov and M. G. Poghosyan, arXiv:0909.5156.

[38] A. B. Kaidalov and M. G. Poghosyan, Eur. Phys. J. C **67**, 397 (2010).

[39] A. Capella, J. Tran Thanh Van, and J. Kweicinski, Phys. Rev. Lett. **58**, 2015 (1987).

[40] N. S. Amelin, E. F. Staubo, and L. P. Csernai, Phys. Rev. D **46**, 4873 (1992).

[41] V. Innocente, A. Capella, and J. Tran Thanh Van, Phys. Lett. **213B**, 81 (1988).

[42] R. Baier, J. Engels, and B. Petersson, Z. Phys. **C2**, 265 (1979).

[43] R. P. Feynman, R. D. Field, and G. C. Fox, Phys. Rev. D **18**, 3320 (1978).

[44] O. V. Kancheli, JETP Lett. **11**, 267 (1970); A. H. Mueller, Phys. Rev. D **2**, 2963 (1970).

[45] Y. V. Kovchegov and K. Tuchin, Phys. Rev. D **65**, 074026 (2002).

[46] A. Kovner and M. Lublinsky, J. High Energy Phys. 11 (2006) 083.

[47] E. Levin and A. Prygarin, Phys. Rev. C **78**, 065202 (2008).

[48] R. D. Field and R. P. Feynman, Nucl. Phys. **B136**, 1 (1978).

[49] L. V. Bravina, L. P. Csernai, P. Levai, N. S. Amelin, and D. Strottman, Nucl. Phys. **A566**, 461c (1994); L. V. Bravina, I. N. Mishustin, J. P. Bondorf, A. Faessler, and E. E. Zabrodin, Phys. Rev. C **60**, 044905 (1999); E. E. Zabrodin, C. Fuchs, L. V. Bravina, and A. Faessler, Phys. Lett. **508B**, 184 (2001).

[50] G. Burau, J. Bleibel, C. Fuchs, A. Faessler, L. V. Bravina, and E. E. Zabrodin, Phys. Rev. C **71**, 054905 (2005); J. Bleibel, G. Burau, A. Faessler, and C. Fuchs, Phys. Rev. C **76**, 024912 (2007); J. Bleibel, G. Burau, and C. Fuchs, Phys. Lett. B **659**, 520 (2008).

[51] G. J. Alner *et al.* (UA5 Collaboration), Phys. Rep. **154**, 247 (1987).

[52] G. Arnison *et al.* (UA1 Collaboration), Phys. Lett. **118B**, 167 (1982); C. Albajar *et al.* (UA1 Collaboration), Nucl. Phys. **B335**, 261 (1990).

[53] F. Abe *et al.* (CDF Collaboration), Phys. Rev. Lett. **61**, 1819 (1988); Phys. Rev. D **41**, R2330 (1990).

[54] T. Alexopoulos *et al.* (E735 Collaboration), Phys. Rev. D **48**, 984 (1993).

[55] K. Aamodt *et al.* (ALICE Collaboration), Eur. Phys. J. C **68**, 89 (2010).

[56] K. Aamodt *et al.* (ALICE Collaboration), Eur. Phys. J. C **68**, 345 (2010).

[57] K. Aamodt *et al.* (ALICE Collaboration), Phys. Lett. B **693**, 53 (2010).

[58] K. Aamodt *et al.* (ALICE Collaboration), Report No. ALICE-PUBLIC-2013-001.
[59] J. Adam *et al.* (ALICE Collaboration), Phys. Lett. B **753**, 319 (2016).
[60] K. Khachatryan *et al.* (CMS Collaboration), J. High Energy Phys. 02 (2010) 041.
[61] K. Khachatryan *et al.* (CMS Collaboration), Phys. Rev. Lett. **105**, 022002 (2010).
[62] V. Khachatryan *et al.* (CMS Collaboration), Phys. Lett. B **751**, 143 (2015).
[63] S. Chatrchyan *et al.* (CMS and TOTEM Collaborations), Eur. Phys. J. C **74**, 3053 (2014).
[64] E. Gotsman, E. Levin, U. Maor, and J. S. Miller, Eur. Phys. J. C **57**, 689 (2008).
[65] E. Gotsman, E. Levin, and U. Maor, Eur. Phys. J. C **71**, 1553 (2011).
[66] M. G. Ryskin, A. D. Martin, and V. A. Khoze, Eur. Phys. J. C **54**, 199 (2008).
[67] M. G. Ryskin, A. D. Martin, V. A. Khoze, and A. G. Shuvaev, J. Phys. G **36**, 093001 (2009).
[68] B. Abelev *et al.* (ALICE Collaboration), Eur. Phys. J. C **73**, 2456 (2013).
[69] G. Antchev *et al.* (TOTEM Collaboration), Europhys. Lett. **101**, 21002 (2013).
[70] R. Aaij *et al.* (LHCb Collaboration), J. High Energy Phys. 02 (2015) 129.
[71] J. Cleymans, J. Strümpfer, and L. Turko, Phys. Rev. C **78**, 017901 (2008).
[72] V. Zaccolo *et al.* (ALICE Collaboration), arXiv: 1512.05273; V. Zaccolo, Ph.D. Thesis, The Niels Bohr Institute, University of Copenhagen, 2015 (unpublished).